Chapter 9

Measurement and Characterization of Gratings

The transfer characteristics of a grating are of primary importance for a number of applications. For example, in high-bit-rate applications, it is necessary to know if the grating will impart additional dispersion and, if so, how much. Gratings can be used in a vast number of demanding applications, such as sensing in harsh environments, or in undersea optical fiber transmission that requires components to survive the 25-year design lifespan of the system. For long-term use, it is essential to know whether or not the grating will maintain its designed characteristics over the lifetime. It is also important to know, as it is for optical fibers, the integrity of its mechanical strength for the same reasons. Thus, reliability is a big issue. The transmission characteristics of certain gratings may be affected by the out-gassing and annealing processes more than others; the resonance wavelengths of *all* gratings drift because of the out-diffusion of molecular hydrogen in high-pressure sensitized fibers. Stress relaxation can complicate matters, by altering the induced refractive index modulation. Sensitivity of the Bragg wavelength with temperature and strain has to be taken into account for such applications as in band-pass filters. Gratings have to be annealed to stabilize their properties for long-term use. The bandwidth, reflection profile, and phase response of gratings require special measurement techniques for proper characterization. In this chapter we shall consider some of the parameters that are of impor-

tance and techniques that have been developed for characterization. These include reflectivity and transmission spectrum, bandwidth, average refractive index change and refractive index modulation coefficient, grating uniformity and quality of apodization, insertion loss, radiation loss, and group delay of chirped gratings, drift due to out-diffusion of hydrogen, temperature effects during measurements, PMD, and stress changes. Methods that have been reported for the measurement of thermal decay of gratings will be covered in the final section. The aim of this chapter is to provide an overview of the properties of optical fibers used for grating fabrication, including thermal annealing and characterization of fiber gratings and mechanical strength.

9.1 Measurement of reflection and transmission spectra of Bragg gratings

The nice thing about gratings is that their growth can be monitored during the inscription process. Since the fabrication is noninvasive, apart from stripping part of the coating, the input and output ends of the fiber are often accessible. Usually the source at the wavelength of interest is an edge-emitting diode, which provides sufficient output power for a variety of measurements. Alternatively, white light may be coupled into the fiber, although the dynamic range is limited. The amplified spontaneous emission from a fiber amplifier is a very good broadband source, and the choice is available to cover the 900–1700 nm wavelength band. It is normal to have either a circulator or a 50:50 fiber splitter between the source and the grating to be measured. The most sensitive method for detecting gratings is in reflection, and for this reason it is best to measure gratings in reflection for diagnostic purposes and display the signal on an optical spectrum analyzer. The basic apparatus for measuring Bragg grating reflection and transmission is shown in Fig. 9.1. The inset shows an alternative arrangement using the coupler.

Reflections just above the noise floor of the spectrum analyzer are easily displayed. When a grating is written into the fiber, a reflection peak appears which may be checked for the wavelength. At the same time, the transmission spectrum shows no change until the grating reflectivity is a few percent. A useful guide is the 3.5% reflection from the cleaved far end of the fiber to calibrate the actual reflection from the

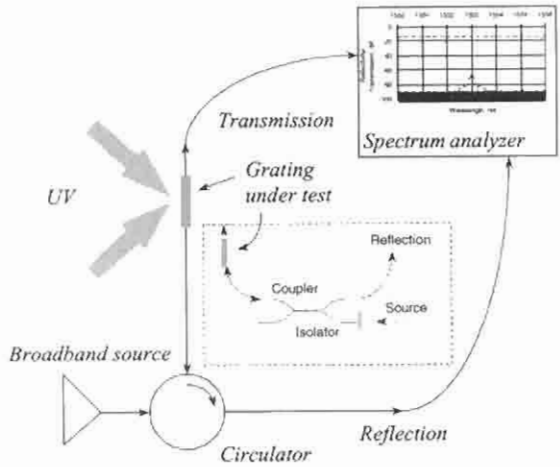

Figure 9.1: Apparatus to measure the transmission and reflection spectrum of Bragg gratings.

grating (see Fig. 9.2). For a uniform grating with a reflectivity R, we can calculate the coupling coefficient, $\kappa_{ac}L$, as

$$\kappa_{ac} L = \tanh^{-1}(\sqrt{R}). \tag{9.1.1}$$

With this information and the measured bandwidth, $2\Delta\lambda$, between the first zeroes (FWFZ), the grating length L is uniquely defined as per Eq. (4.6.14),

$$2\Delta\lambda = \frac{\lambda^2}{\pi n_{eff} L} \sqrt{(\kappa_{ac}L)^2 + \pi^2}. \tag{9.1.2}$$

From the length, we may calculate the refractive index modulation $\nu\overline{\Delta n}$ as in Eqs. (4.6.3) and (4.3.6), with a fringe visibility ν,

$$\kappa_{ac} = \frac{\pi\eta\nu\overline{\Delta n}}{\lambda}. \tag{9.1.3}$$

Eqs. (9.1.1) and (9.1.2) are plotted in Fig. 9.3 for three different values of grating length, 1, 2, and 8 mm, as a function of the coupling constant κ_{ac}. The data has been plotted for a Bragg wavelength of 1550 nm. The wavelength shift $\delta\lambda$ as the grating grows can be calculated from Eq. (4.6.4),

$$\delta\lambda = 2\lambda\eta \frac{\Delta n}{n}, \tag{9.1.4}$$

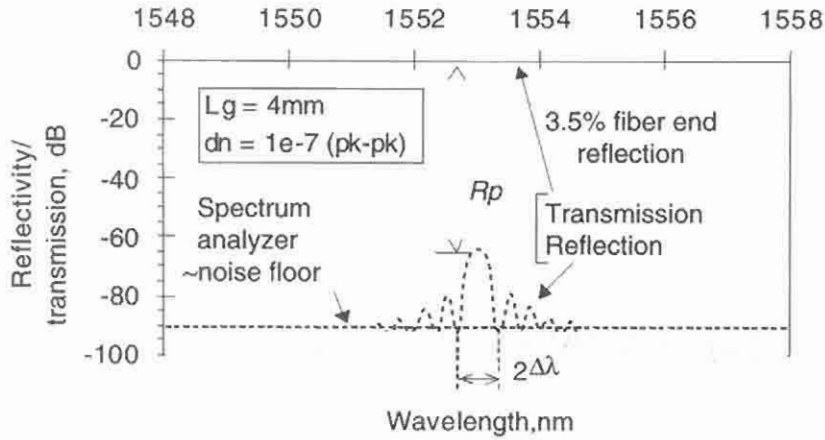

Figure 9.2: The reflection spectrum of a 4-mm-long grating with a refractive index modulation amplitude of only 10^{-7}. At this stage it is undetected in transmission. Also shown is the ~3.5% reflection from the cleaved end of the fiber, assuming that there are no losses in the reflected light. The very weak Bragg reflected signal is easily detected. The noise floor for a spectrum analyzer resolution of 0.1 mm is shown only as an example.

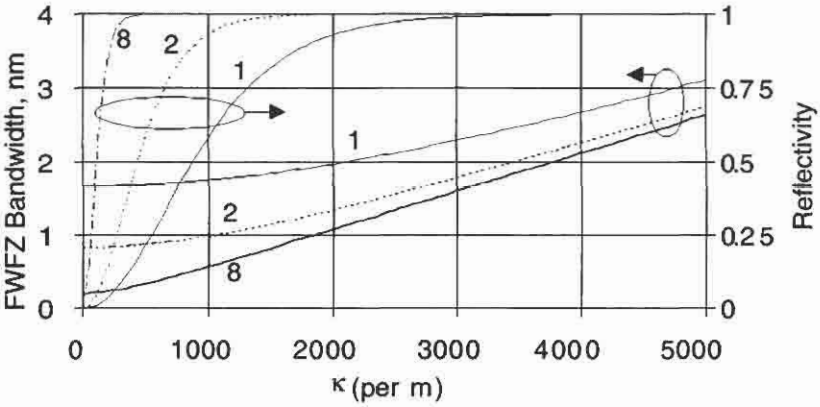

Figure 9.3: The reflectivity and bandwidth of three Bragg gratings as a function of the coupling constant κ_{ac} at a wavelength of 1550 nm. The numbers refer to the lengths in millimeters. Note that for large values of the coupling constant, the grating bandwidth grows linearly. As a guide, the maximum refractive index modulation amplitude, Δn, for $\nu = 1$, and overlap, $\eta = 0.8$, is $\sim 3 \times 10^{-3}$ (at $\kappa_{ac} = 5000\ \mathrm{m}^{-1}$).

where we remind ourselves that Δn is the ac index change and λ is the Bragg wavelength at the start of the growth of the grating.

As the grating grows, it shifts to longer wavelengths and this is shown in the transmission spectra in Fig. 9.4. Along with the shift is shown the effect of a nonuniform UV beam profile. This has been assumed to have a Gaussian profile, as with many laser beams, and causes a chirp in the grating [1], since the Bragg wavelength is proportional to the effective mode index. There are two effects of the nonuniform UV beam profile: The grating acquires additional structure on the short-wavelength side (Fig. 9.4) as it grows, and the peak reflectivity drops for the same refractive index modulation amplitude, as is seen for the uniform profile grating in Fig. 9.5.

Comparing the uniform and the Gaussian intensity profile grating, the effect on the bandwidth is only slight. The long-wavelength edge of the Gaussian profile grating is apodized.

We now compare the Gaussian intensity profile with the Gaussian apodized grating, i.e., one in which the refractive index modulation changes with the length of the grating, but not the mode effective index (see Chapter 5), and find that the short-wavelength structure disappears and the peak reflectivity increases with apodization. The reason for this is that the Bragg wavelength of the apodized grating is constant and the

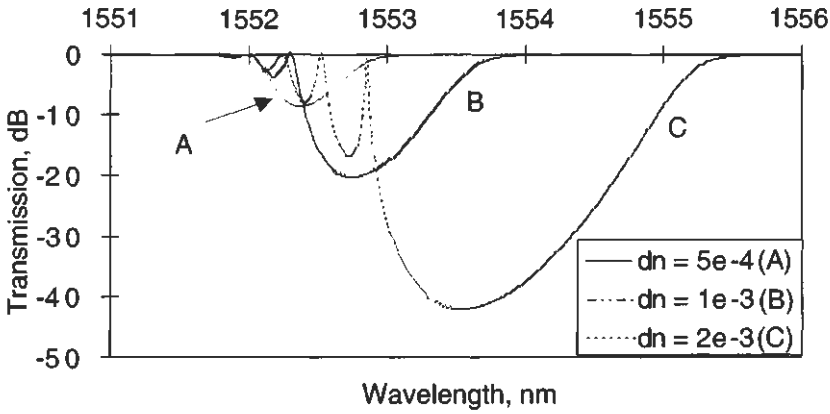

Figure 9.4: The shift in the Bragg wavelength and the appearance of the Fabry–Perot structure on the short-wavelength side of a Gaussian intensity profile grating as the UV-induced refractive index modulation amplitude increases.

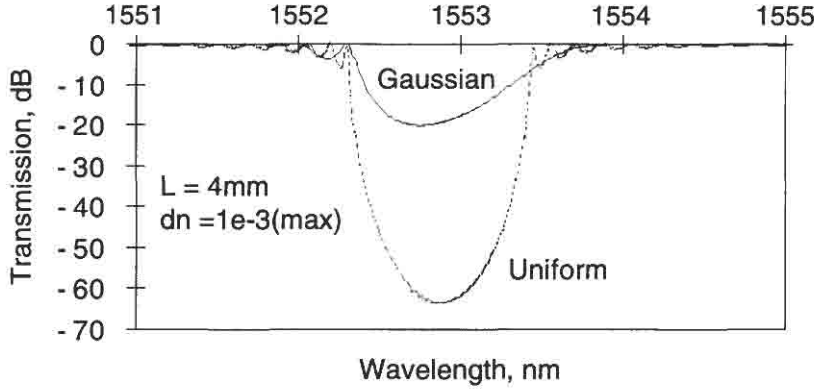

Figure 9.5: A uniform amplitude profile grating compared with a Gaussian amplitude profile grating.

reflection is not spread over a larger bandwidth, and so the effective length is longer. (See Fig. 9.6.)

The maximum reflectivity can be calculated by measuring the transmission dip T_d in dBs. The translation from the measured dip to the reflectivity is

$$R = 1 - 10^{-T_d/10}, \tag{9.1.5}$$

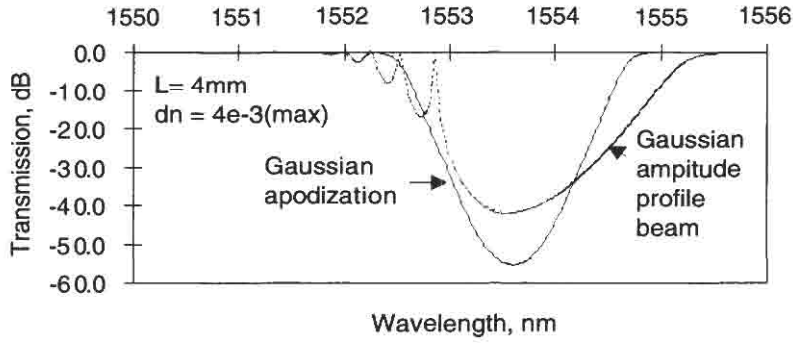

Figure 9.6: Comparison of chirp induced in a strong grating due to the amplitude profile of the writing beam and a Gaussian profile apodized grating with the same parameters. The FWFZ bandwidth is approximately the same, but the slope on the long wavelength side is different, as well as the structure on the short wavelength side.

or from the peak of the reflected signal R_p below the transmitted signal it is (as shown in Fig. 9.2)

$$R = 10^{-R_p/10}. \tag{9.1.6}$$

The data is shown in Fig. 9.7. For example, in Fig. 9.2, the reflected signal is shown to be ~70 dB below the transmission level. This translates to a reflectivity of 10^{-5}%.

Alternatively, a 10-dB transmission dip is equivalent to a reflectivity of 90%, 20 dB is 99%, and so on. It is assumed that there is no additional loss in the reflected signal as compared with the transmitted signal. If the loss is known, the transmitted level or the reflection peak must be adjusted accordingly.

Special care needs to be taken when measuring transmission dips in excess of ~30 dB because of the limited resolution of the spectrum analyzer. The slit width of the spectrum analyzer is not a delta function, and there is substantial leakage from the spectral region outside of the slit bandwidth. Integrated, it amounts to more signal being transmitted and affects the spectrum mostly at the dip in the grating transmission. There are several solutions to this problem. Obviously, a better spectrum analyzer is one, or a tunable laser source may be used in conjunction with a conventional spectrum analyzer, ensuring that the scanning of the laser and the spectrum analyzers are synchronized [2] with an appropriate slit width. The combined side-mode suppression and the slit width reduces

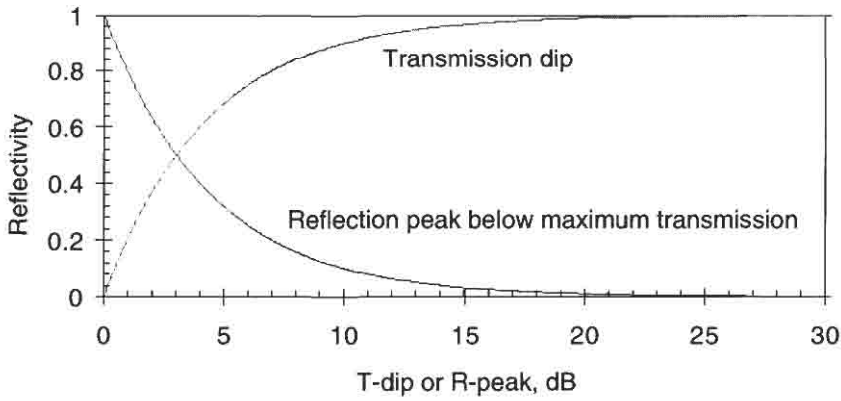

Figure 9.7: Reflectivity as a function of the dip in the transmission spectrum of a grating or as the reflection peak below transmitted signal.

the captured noise. Such a measurement is shown in Fig. 9.8, in which the spectrum of a strong 4-mm-long grating spectrum with a transmission dip of >60 dB has been resolved. In addition to the very steep long-wavelength edge, it has structure on the short wavelength that is due to cladding mode coupling and Gaussian chirp.

Clearly, chirp is not a feature that is desirable for simple transmission filters. We now consider the spectra of uniform period gratings and the effect of apodization. Figure 9.9 shows the reflection spectrum of unapod-

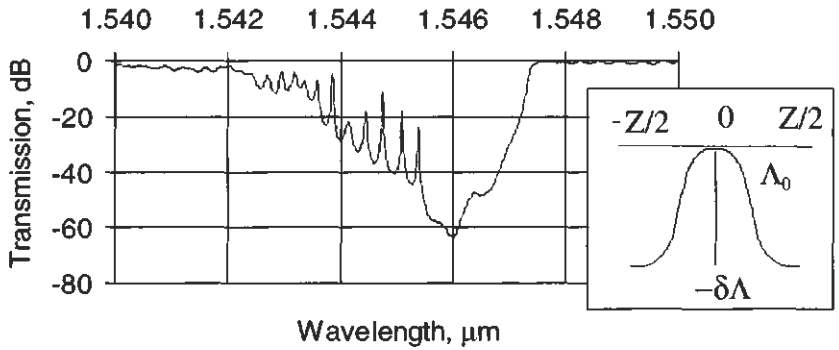

Figure 9.8: The measured grating is ~4 nm long with an estimated index modulation of 4×10^{-3}. The beam intensity profile had a Gaussian shape. The inset shows the change in the Bragg wavelength across the length of the grating.

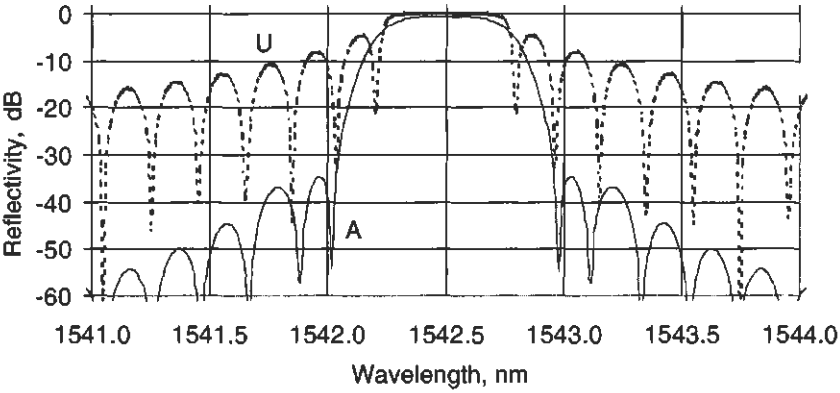

Figure 9.9: Reflection spectra of 4-mm-long unapodized and $\cos^2$ apodized gratings with a refractive index modulation amplitude of 4×10^{-4}.

ized and apodized ($\cos^2$ profile) gratings. The unapodized grating is nominally a 100% reflection grating, and the apodized one has identical length and refractive index modulation. The effect of apodization is to reduce the effective length to approximately $L/2$. As a result, the FWFZ bandwidth approximately matches the second zeroes of the unapodized grating. Note that the reflectivity is also reduced (~halved). To generate an apodized grating with the same bandwidth, the length has to be approximately doubled, and the coupling constant has to be adjusted, so that an 8-mm-long raised cosine apodized grating will have the same approximate bandwidth and reflectivity.

In order to resolve the reduced side lobes for the apodized grating, the spectrum analyzer linewidth should be selected to remove artifacts and a false noise floor.

9.2 Perfect Bragg gratings

It is possible to make very high-quality uniform-period Bragg gratings. This is because optical fiber has very uniform properties. The theoretically calculated reflection, along with the measured spectrum, of a 30-mm-long grating is shown in Fig. 9.10. The grating was fabricated by scanning a phase mask with a UV beam [3].

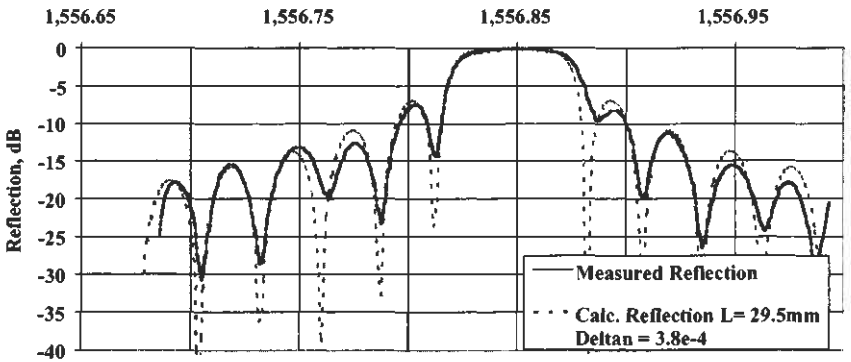

Figure 9.10: Measured and computed reflection spectrum of a 29.5-mm-long fiber Bragg grating, produced by the scanned phase-mask technique [4]. The uniformity of the grating is indicated by the close agreement between the zeroes of the theoretical and measured response.

The agreement between measurement and theory is very good, with the zeroes matching across almost the entire spectrum shown. Notice the slight deviations, especially at the first side-lobe zero (RHS), and the third side-lobe zero (LHS). These features are indicative of slight chirp and nonuniformity in the writing process. Nevertheless, this grating has ~28,000 grating periods and shows a near-ideal response. One way to measure such a narrow bandwidth is to use a high-quality tunable laser source and a spectrum analyzer for reasons of resolution. It is difficult to measure such gratings accurately in transmission with a broadband source, since the bandwidth is almost the same as that of commercially available optical spectrum analyzers (0.07 nm FWHZ). Although this grating has a transmission dip of ~14 dB, the spectrum remains unresolved in transmission with a spectrum analyzer.

Gratings with such performance are particularly useful where the phase response is required along with the reflection characteristics in filtering applications, such as in pulse shaping and dark soliton generation [4].

9.3 Phase and temporal response of Bragg gratings

Figure 9.11 shows the computed reflection and accumulated phase-spectrum of a uniform-period unapodized Bragg grating. The measurement of phase of a grating can only be made by the measurement of the grating's complex amplitude reflectivity. A technique has been proposed for the reconstruction of the phase of the grating using arguments based on causality and minimum phase performed on the measured reflection spectrum of a grating, with reasonable success [5]. This may be done by using interferometric techniques to characterize weak gratings (<20% reflectivity) [6–9]. These measurements have at best limited spatial resolution, or are difficult to implement, being interferometric. Other more direct methods include the use of a network analyzer for the measurement of dispersion [10,11]. The use of the network analyzer relies on the dispersion being constant over the frequency region of interest, and strictly it is better suited to measuring apodized chirped gratings. This technique has been applied to gratings to measure their dispersion [12,13]. Another method for testing of a grating or phase mask uses a probe transverse to the grating [14].

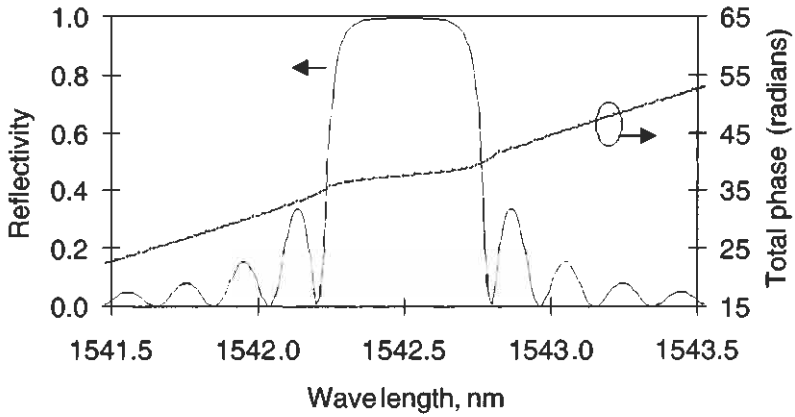

Figure 9.11: The reflectivity and phase of a 4-mm-long unapodized grating with a refractive index modulation amplitude of 4×10^{-4}.

Typically, the accumulated phase for a 4-mm-long grating is a few tens of radians, as shown in Fig. 9.11.

The group delays of the two gratings used for Fig. 9.9 are shown in Fig. 9.12. The strong dispersion at the edges of the band stop limits the useful bandwidth of a band-pass filter, especially in high-speed applications [15,16]. In Ref. [16] asymptotic expressions may be found for the

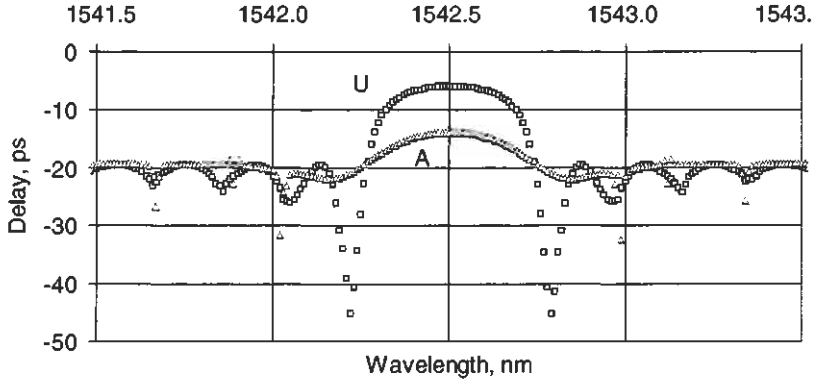

Figure 9.12: Dispersion of 4-mm-long unapodized (U) and apodized (A) gratings.

dispersion on the long-wavelength side of the band stop of apodized gratings, useful for dense DWM systems. Note that the dispersion at the band edge of the grating reaches several tens of picoseconds for the unapodized grating and is much reduced in the apodized grating. Despite the apodization, there is a curvature in the center of the band stop, which may be useful to compensate for the chirp of a source [15].

The group delay shown in Fig. 9.12 is for gratings with uniform characteristics. Often there is a chirp involved, which has a significant effect on the dispersion. We note that the group delay characteristics of the uniform gratings remain symmetric about the center of the bandgap. With chirp in a grating, the group delay changes sign on one side of the band stop, and this is shown in the calculated response in Fig. 9.13. The unapodized grating acquires less pronounced zeroes and the group delay, a point of inflection.

To characterize the group delay of gratings, a measurement setup based on the vector-voltmeter [17] is shown in Fig. 9.14. In this method, light from a tunable single-frequency source is modulated at a frequency f and is launched into a grating under test. The reflected (or transmitted) signal is compared via a circulator with the modulated input signal in a vector voltmeter. As the wavelength of the source is tuned, the delay in the reflected light from the grating changes. The vector-voltmeter compares the phase of the modulated light and translates it into a phase difference. Thus, the phase at the modulated frequency f is measured.

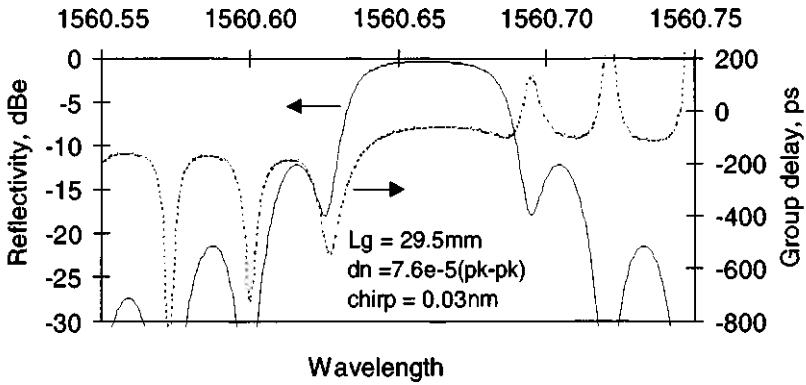

Figure 9.13: Simulated response of a 29.5-mm-long grating with a 0.03-nm chirp and refractive index modulation of 7.6×10^{-5} (peak-to-peak).

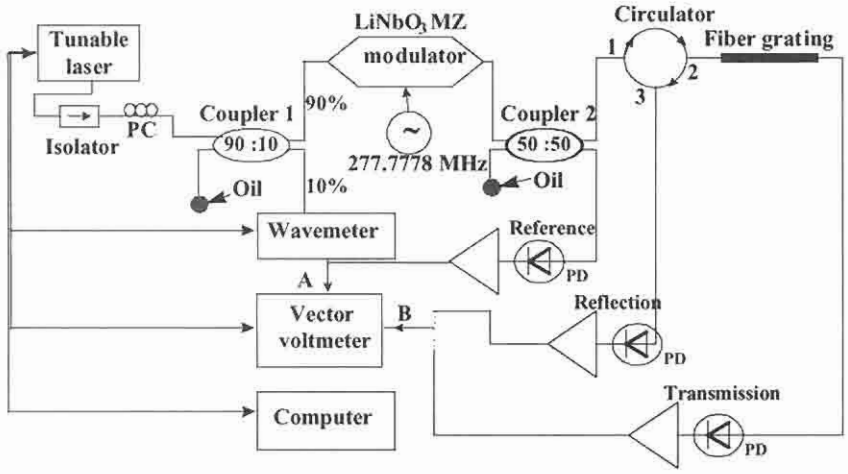

Figure 9.14: A schematic of the apparatus for the measurement of group delay, reflectivity, and transmission of gratings (after Ref. [17]).

With a judicious choice of the modulation frequency, e.g., 277.77778 MHz, one degree of phase change is equivalent to a delay τ of 10 psec, as [18]

$$\tau = \frac{1}{360f} \text{ sec deg}^{-1}. \tag{9.3.1}$$

Under computer control, this data may be acquired quickly with a minimum of processing. The resolution of the measurement may be increased by increasing the modulation frequency, but it is nominally ~1 psec or better. With such a resolution, care needs to be taken, since temperature variations during the course of the measurements can cause errors. Changes in the path lengths of the fiber used in the setup and also in the polarization affect the measurement. It is for these reasons that the paths are kept to a minimum and a reference frequency is generated optically after the modulator. Any amplitude and phase changes are then common to both the reference and the signal, minimizing errors.

The reflection and group delay of a 30-mm-long grating of the type shown in the simulation of Fig. 9.13 are shown in Fig. 9.15. We note that the similarity is striking between the two grating spectra, in both reflectivity and group delay. It is therefore possible to characterize the measured spectra using simple simulation, since fiber-grating spectra can be so good. Note that the reflectivity spectra is in dB (electrical) = 2 ×

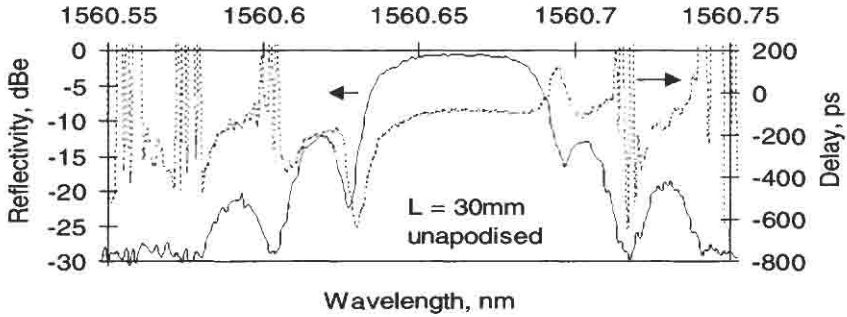

Figure 9.15: The spectra of a 30-mm-long grating measured using the vector voltmeter.

dB (optical). The grating reflectivity can be measured in transmission, to normalize the peak of the reflectivity spectra. The results for an identical but apodized grating are equally good.

We now move on to the spectrum of a longer grating, of the type used in dispersion compensation. There are a few points that need to be remembered. In Chapter 7 the delay response of long gratings is considered in detail, and it is found that long gratings need to be characterized with high wavelength resolution if the GDR (group delay ripple) spectrum is to be resolved. In making measurements, a wavelength resolution of 1 pm is generally sufficient. The measured reflectivity and group delay of a raised cosine apodized, 100-mm-long grating is shown in Fig. 9.16. The

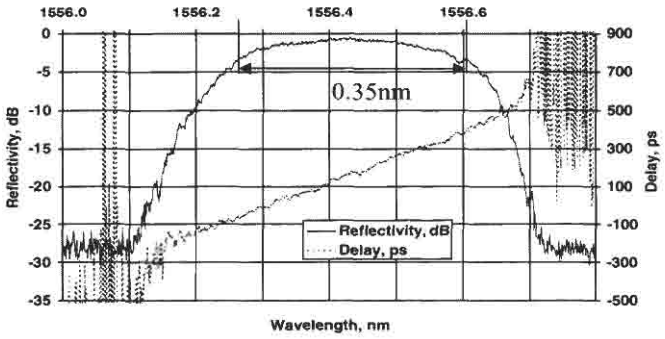

Figure 9.16: The reflectivity and delay of a 100-mm-long chirped grating with a chirped bandwidth of 0.75 nm [19], measured with a resolution of 1 pm.

data has been measured with 1 pm resolution, and the GDR is adequately resolved. We can measure the 3-dB optical (6-dBe) reflectivity bandwidth by comparing the transmitted signal level with R_p, remembering that the measurements are in dBe.

This grating is designed to compensate the dispersion for ~80 km of standard optical fiber, as has been presented in Chapter 7. With unapodized gratings the low resolution masks the detail and a comparison is shown in Fig. 9.17. Here two measurements of the same grating made with 10 pm and 1 pm are compared. The GDR is apparent with the higher resolution. With longer gratings this factor becomes even more critical.

As we have seen in Chapter 7, for 1-meter-long unapodized gratings, the GDR frequency has a period of ~1.5 pm. To resolve the GDR, other means have to be adopted, such as the use of a multisection DFB laser [17], which can be electrically tuned. This is a very time-consuming task, since other factors such as the ambient temperature need to be controlled very accurately. The drift of the wavelength with temperature of a chirped grating is an issue. The grating should be temperature controlled in order to get an accurate measurement. With a change in the local Bragg wavelength of several pm/°C, a stable environment is essential for the measurement.

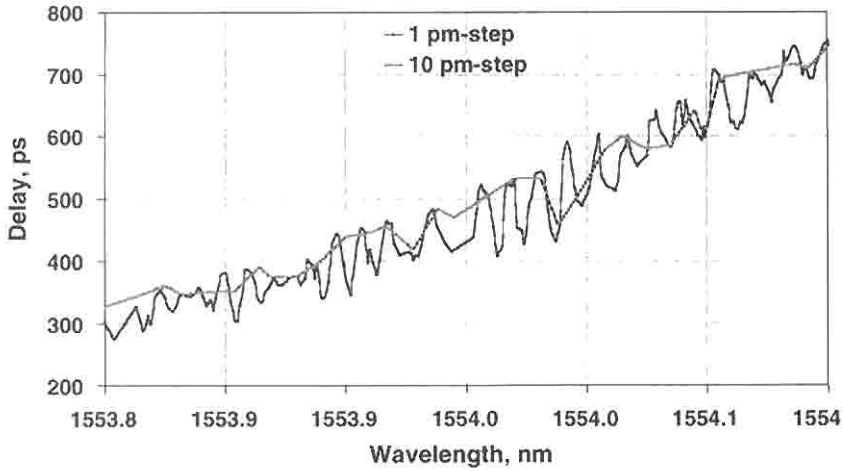

Figure 9.17: Resolution dependence of the group delay of an unapodized chirped grating (after Ref. [17]).

Finally, we consider the drift of the Bragg wavelength with the out-diffusion of hydrogen for a fiber after the grating has been written. With a typical period of measurement of tens of minutes to an hour, the out-diffusion of hydrogen (or deuterium) must be taken into consideration, as has been shown in Chapter 2 [20,21]. In Fig. 9.18 we see the drift in the Bragg wavelength of a chirped grating monitored over a period of 45 days from the inscription of the grating, immediately after removal from the cold storage. The fiber is deuterium soaked at 200 bar at the start. By the end of 45 days, the total drift in the wavelength is approximately -1.65 nm, and it continues to shift very slowly.

With technological improvements, it will be necessary to measure even longer gratings, perhaps longer than 10 meters. The measurement of one of these gratings (reflection spectrum of a 2-meter-long WDM channelized grating is shown in Fig. 9.19) can take several hours at picometer resolution. Here it becomes important that the grating be collectively maintained at the same temperature for the duration of the measurement.

A fast technique has been reported by Ouellette *et al.* [22], which relies on the intrinsic birefringence B of the fiber. By alternately measuring the orthogonal polarization reflected, $S2$, and launched, $S1$, signals from the spectrum analyzer, the group delay is shown to be

$$\tau = \frac{n\lambda}{4\pi Bc} \cos^{-1}\left(S1 - \frac{S2}{S1} + S2\right). \tag{9.3.2}$$

This method requires the calibration of the fiber birefringence. This technique may prove to be valuable, since it is simple, although there is no information available on the resolution.

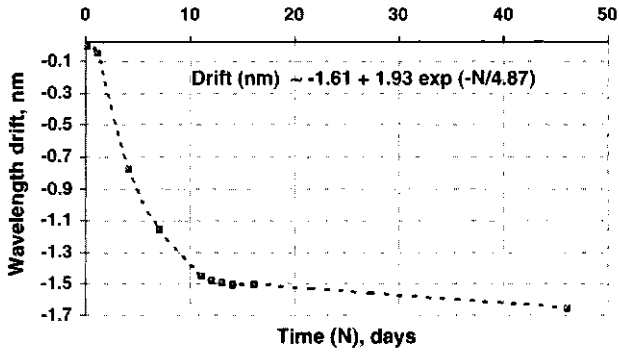

Figure 9.18: The drift in the Bragg wavelength of a chirped grating with time due to deuterium out-diffusion [17].

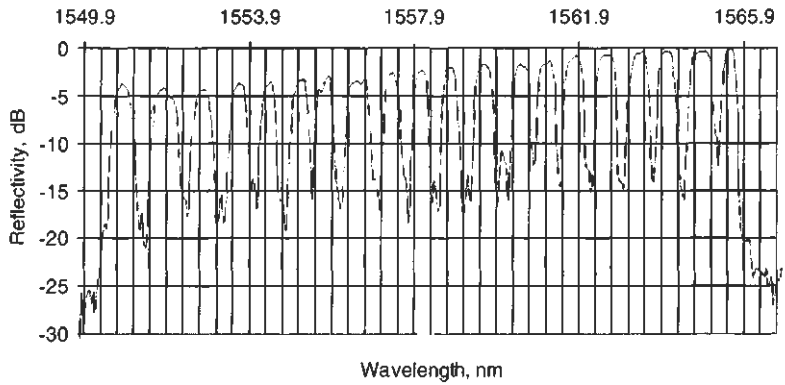

Figure 9.19: The reflection spectrum of a 2-meter-long grating fabricated at BT Laboratories. Both radiation and loss due to deuteration reduce the reflected signal from the shorter wavelength gratings. The combined loss of deuteration and radiation is 2 dB/m [26].

We remind ourselves that for the dispersive properties of gratings with a reflectivity of between 10 and 15 dB, the time delay τ may be calculated as

$$\tau = \frac{2n_{eff}L_g}{c}, \tag{9.3.3}$$

where L_g is the length of the grating and c is the speed of light. For a signal pulse with a transform-limited bandwidth, $\Delta\lambda$ equal to the bandwidth of the grating chirp, the dispersion can be simply described as

$$D = \frac{2n_{\text{eff}}L_g}{c\Delta\lambda} = \frac{2L}{\nu_g\Delta L}, \tag{9.3.4}$$

where L is the physical length of the grating, and ν_g is the group velocity of the pulse. The effects of dispersion can be considerable even in a short grating since the group delay in a fiber is 5 nsec m^{-1}, and in reflection it is doubled.

We have seen in Chapter 7 how PMD can affect the GD of gratings. The measurement of PMD, or rather birefringence, can be made simply by launching light along the two orthogonal birefringent axes of the fiber grating and observing the wavelength shift. Meltz and Morey [23] reported a birefringence-induced Bragg wavelength shift of ~0.1 nm, equivalent to an induced birefringence at 1550 nm of $\sim 2.3 \times 10^{-5}$. This value is high

and the Bragg wavelengths are therefore easily separated in a spectrum analyzer. By rotating the polarization of the UV writing beam so that it is along the fiber axis, the UV-induced birefringence can be reduced from ~5% of the UV-induced refractive index change to around 0.5% [24]. This area has received more attention recently, with the application of setup similar to that shown in Fig. 9.14 to measure the group delay difference of two polarization states. Also applied is the Jones matrix approach to map out all the polarization states in the fiber. The comparison between the two methods is good. Measured polarization-induced delay is reported to be ~28 and 7 psec for two chirped gratings written in different fiber [25].

Clearly this is an area that will receive attention as the deployment of fiber gratings for dispersion compensation becomes widespread.

9.3.1 Measurement of the grating profile

The use of simulation is an excellent method for characterizing the measured spectrum of a grating. By knowledge of the physical length, the reflectivity and the shape of a grating, it is possible to identify a couple of parameters to choose in order to allow the simulation. This has been demonstrated for the spectra shown in Figs. 9.13 and 9.15. More complex structure can be analyzed theoretically, as has been amply demonstrated by Ouellette *et al.* [27] for stitching errors produced by phase masks. For example, random errors in the stitching cause the bandwidth of a uniform-period grating to broaden and acquire noise. The errors can be calculated from the simulation. Alternative techniques exist for assessing the refractive index profile of a grating. These include optical low-coherence reflectometry (OLCR), originally used to detect small flaws in optical waveguides [28,29], applied to fiber gratings by Lamblet *et al.* [30], and the method of side scatter from a grating, demonstrated by Krug *et al.* [31]. An interesting and very simple technique is the application of "heat scan" to probe the chirp in a grating [32,33]. The grating is probed with a fine hot wire while the reflection characteristics are being monitored. A detuning of the Bragg wavelength as a function of probe position measures the chirp. These are in addition to other methods already mentioned as being appropriate for assessing phase masks [9,14]. It is important to know the sources of "noise" on a grating, or correct for a flaw [34–36], since the out-of-band spectra may deteriorate. It should be mentioned that optical time-domain reflectometry (OTDR, or back-scatter) has also

been used to locate gratings. In the next section we will consider the OLCR method and side-scatter as two techniques to assess Bragg gratings.

Optical low-coherence reflectometry

The scheme is based on a fast scanning Michelson interferometer, with the grating as the mirror in one arm, and a scanning broadband mirror (BBM) in the reference arm. Reflected light from the grating and the mirror interferes at a photodiode. The source has a large bandwidth so that the coherence length is short, and therefore interference is only visible over a short region of the grating when the path lengths are within the coherence length. The path difference between the arms is adjusted by moving the reference mirror so that different points within the grating are sampled. A schematic of the apparatus is shown in Fig. 9.20 [37]. The moving reference mirror is mounted on a motorized stage with a long scan length to allow easy adjustment of the paths. The phase modulator is provided to derive a lock-in signal. With reference to a 100% reflection, a cleaved end with approximately 4% end reflection registers a signal at −14 dB. The measurement has range with a noise floor at −140 dB with a bandwidth of 1 Hz.

The source should have low spectral ripple to avoid artifacts. The coherence length, and therefore the resolution of the measurement in the fiber is

$$l_c = \frac{4 \ln 2}{\pi} \frac{\lambda^2}{\Delta\lambda_{FWHM}}, \tag{9.3.5}$$

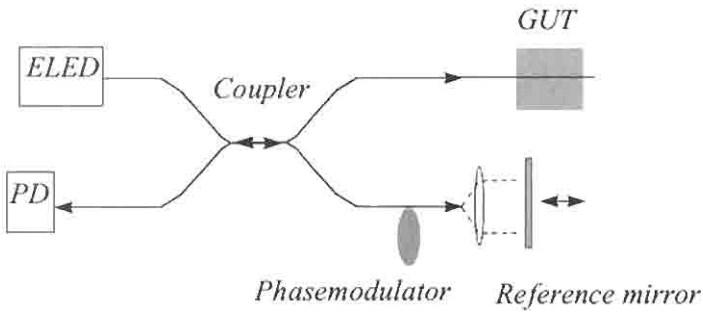

Figure 9.20: A schematic of the OLCR apparatus (after Ref. [37]).

where $\Delta\lambda_{FWHM}$ is the source linewidth and λ is the center wavelength, and the resolution $R = l_c/2n$ where n_g is the group index. For $\Delta\lambda_{FWHM}$ = 55 nm at λ = 1300 nm, we get l_c = 18.3 μm and hence R = 9.1 μm.

The grating spectra are recorded by scanning the reference mirror. In a modified version of the setup, a rotating corner cube is used for increasing the speed of data acquisition. A typical OLCR spectrum is shown in Fig. 9.21. Here the front end reflection is followed by a decay in the signal with penetration depth; this is followed by another increase in the signal as the light exits the far end of the grating at a distance z = 1.222 mm, equivalent to a physical length of z/n_{eff} = 0.84 mm.

The exponential decrease in the signal is proportional to the strength of the grating, while the initial fast rise at the entrance and soon after the first exponential decay is due to the abrupt starting and ending of the grating — a top-hat function. The further oscillations observed are due to the Fabry–Perot modes as the light rattles around within the grating. The measured spectra are the Fourier transform of the product of the amplitude reflectivity of the grating and the spectral distribution of

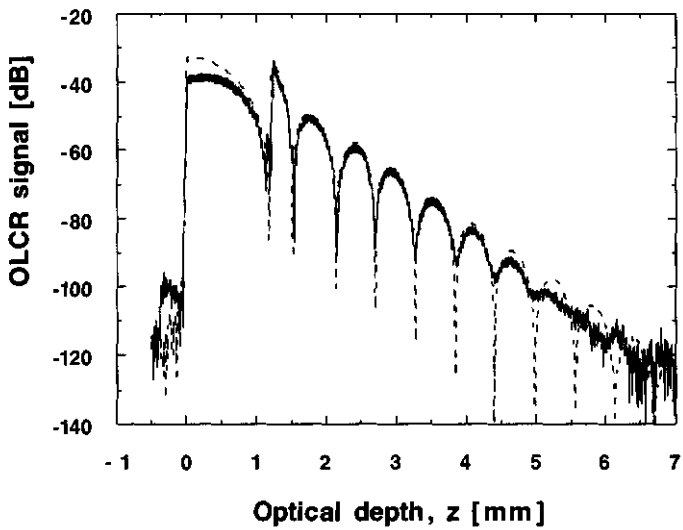

Figure 9.21: The OLCR spectrum of a 0.84-mm-long grating (courtesy Hans Limberger from: Lambelet P, Fonjallaz P Y, Limberger H G, Salathé R P, Zimmer C and Gilgen H H, "Bragg Grating Characterization by Optical Low-Coherence Reflectometry", *IEEE Phot. Technol. Lett.*, 5, 565–567, 1993. © 1993 IEEE.[30]).

the source. The free parameter is the refractive index modulation of the sinusoidal period, since the Bragg wavelength is known, and the length of the grating is found from the length of the scan between the start of the spectrum and the reflection at the end of the grating. The zeroes of the OLCR spectrum are a very sensitive function of the refractive index modulation amplitude, and therefore provide an accurate value. The inverse Fourier transform of the OLCR data and deconvolution of the source spectrum give the grating spectrum. This is shown with the measured grating reflection spectrum in Fig. 9.22. The agreement is altogether excellent.

This technique has been applied by Malo *et al.* [38] to measure the profile of an apodized grating. It is claimed that the relative precision with which the refractive index modulation may be measured is around 1% [30].

Side-scatter measurements

Bragg gratings scatter radiation out of the fiber both within and outside of the bandgap. This is due to a number of reasons, not least radiation

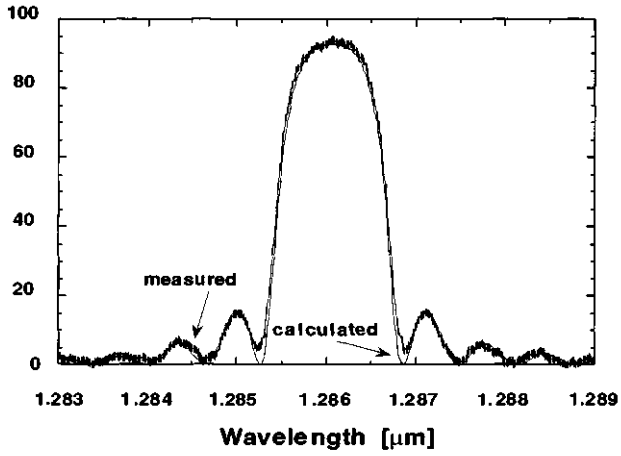

Figure 9.22: Measured and calculated reflection spectra (from the data obtained by OLCR measurement; see Fig. 9.21) as a function of wavelength for an in-fiber grating with a period of 0.443 μm, a length of 0.84 mm, and a modulation depth of $\Delta n = 1.16 \times 10^{-3}$ (courtesy Hans Limberger from: Lambelet P, Fonjallaz P Y, Limberger H G, Salathé R P, Zimmer C and Gilgen H H, "Bragg Grating Characterization by Optical Low-Coherence Reflectometry", *IEEE Phot. Technol. Lett.*, 5, 565–567, 1993. © 1993 IEEE. [30]).

mode coupling of light into the cladding, which can be detected easily [39]. The writing process causes an asymmetry, which assists a directional coupling to the cladding modes (see Chapter 4). Apart from the coherent scattering mechanism, there is also in coherent scatter due to damage in the core as in a Type II grating [40]. This type of grating scatters light because of large surface irregularities at the core–cladding boundary. A third type of scattering mechanism is incoherent and is due to the inhomogeneity in refractive index modulation through the length of the grating. The latter has been investigated by Janos *et al.* [41]. There appears to be a pronounced scatter out of the fiber perpendicular to the direction of the writing beam. The observed anisotropy is consistent with the production of "scattering elements" within a few microns of the core. The scattering loss ranges from 0.2 dB/cm in highly doped Yb/Er phosphosilicate fiber with gratings inscribed with a pulsed laser 193-nm source, to 5×10^{-5} dB/cm for a boron-codoped fiber with a CW 244-nm source.

A technique that measures the sideways diffraction from a fiber Bragg grating is used to characterize the grating refractive index profile. A schematic of this method is shown in Fig. 9.23. In this arrangement, light from a He–Ne laser is focused form the side of the fiber, incident at an angle θ_i to the normal. The schematic of the side-scatter measurement is

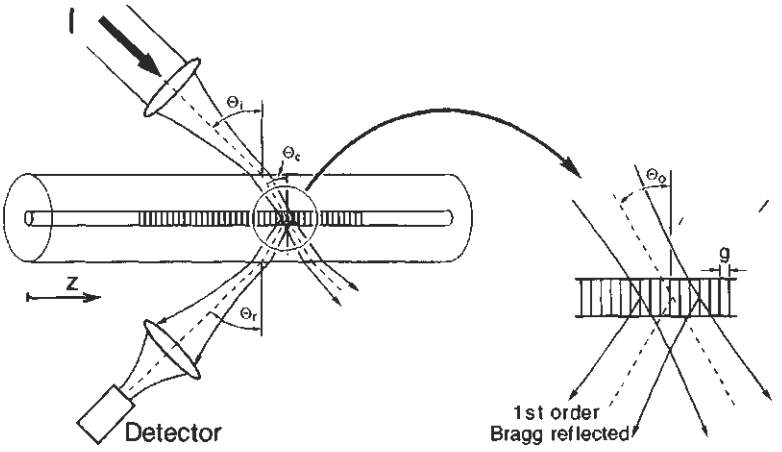

Figure 9.23: The side-diffraction scheme for characterizing Bragg gratings (from: Krug P, Stolte R and Ulrich R, "Measurement of index modulation along an optical fiber Bragg grating", *Opt. Lett.*, **20**(17), 1767–1769, 1 September 1995. [31]).

shown in Fig. 9.23. As has been seen in Chapter 3 on fabrication of gratings with a phase mask, the incident light must have a wavelength less than the period of the grating in the fiber in order to have a first-order diffraction. Referring to Fig. 9.23, which defines the angles, and from phase matching conditions, we find [31]

$$\sin\,\theta_r = \sin\,\theta_i = n_{clad}\sin\,\theta_{clad} = n_{core}\sin\,\theta_{core} = n_{eff}\frac{\lambda_{probe}}{\lambda_{Bragg}}, \qquad (9.3.6)$$

where n_{eff} is the effective index of the fiber at the probe wavelength, so that the probe wavelength must be greater than the Bragg wavelength of the grating by a factor of the effective index of the fiber. The input light is reflected at the incident angle, θ_i. In the weak scattering limit, the cross-section σ_i (as fraction of the incident peak-power density) is given by the following expression, assuming that the grating has a pure sinusoidal period [31], and the focused spot size w_i in the core is much greater than the core radius a:

$$\sigma_i \approx 1.66k^2a^3w_i\Delta n^2\frac{\sin^2\gamma_{core}}{\cos^2\theta_{core}}. \qquad (9.3.7)$$

Here Δn is the local refractive index modulation amplitude, k is the wave vector at the incident wavelength λ_{probe}, and γ_{core} is the angle between the reflected and incident beams and ignores reflection losses. Owing to the geometry of the scattering region, γ_{core} is polarization sensitive and s-polarized light; the reflected power is maximum at $\gamma_{core} = \pi/2$.

Typical parameters used for the experiment are a beam waist of 5 μm, using a 10-mm focal length focused ~37 μm in front of the surface of the fiber to give a spot size of approximately 10 μm at the core (after focusing from the core–cladding surface) with an incident angle of 45.3°. The equivalent internal angle $\theta_{core} = 29.4°$. The input power needs to be high for a good signal-to-noise ratio, and was reported in the experiments to be 5 mW. The resolution in this arrangement is limited to the spot size of 10 μm.

The fiber grating is scanned in front of the fixed laser beam, so that the data may be recorded as a function of position along the grating. Good correlation between the measurement and the simulated transmission spectrum of the grating has been reported [31,35]. The side-diffraction profile of a Gaussian apodized grating is shown in Fig. 9.24. From this profile, it is simple to simulate the grating transfer function to establish a correlation.

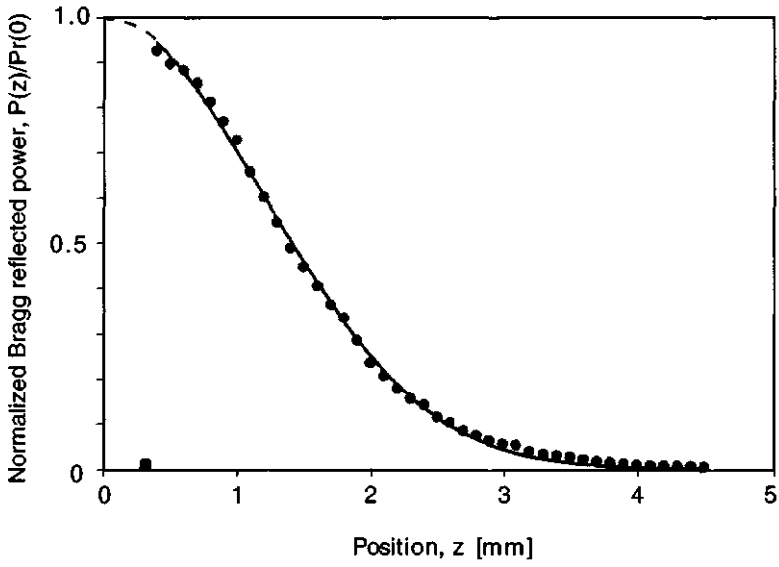

Figure 9.24: The profile of the light diffracted from a Bragg grating using the side-diffraction scheme (from: Krug P, Stolte R and Ulrich R, "Measurement of index modulation along an optical fiber Bragg grating", *Opt. Lett.*, **20**(17), 1767–1769, 1 September 1995. [31]).

The assumption of Eq. (9.3.7) restricts the application of this technique to gratings with *slowly* varying chirp by a variation of the grating period and to average refractive index ($\delta\lambda/\Lambda < 1^{-3}$), with no saturation in Δn. The chirp is limited by the numerical aperture of the focused beam.

Figure 9.25 shows the refractive index modulation profiles of four gratings commonly encountered in Bragg grating technology.

9.3.2 Measurement of internal stress

The refractive index changes induced by UV irradiation appear to affect the internal stress in the core [42]. There are conflicting observations, both of which are supported by experimental evidence [43]. In this section we consider the measurement of internal stress by optical means [44,45]. The technique is simple and requires the measurement of the state of the polarization of a focused spot of light (typically 3 μm diameter) transversely incident on the fiber, as it is scanned through the core region,

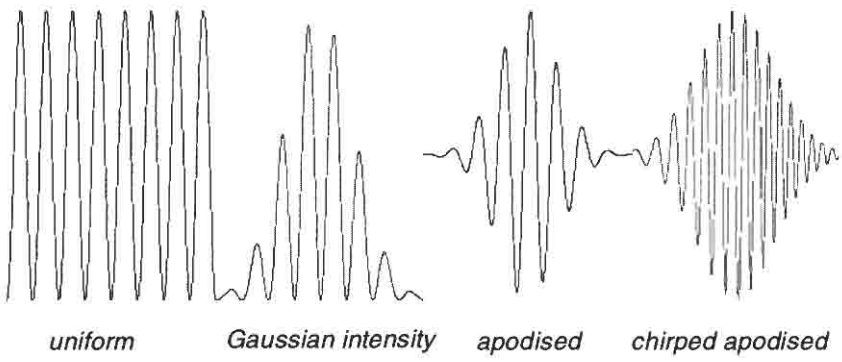

Figure 9.25: Four commonly encountered grating refractive index modulation profiles.

implemented by Fonjallaz *et al.* [46]. It therefore is a polarimetric measurement, which requires the polarization of the incident beam to be at 45° to the orthogonal birefringent axes of the fiber. The fiber is immersed in index-matching fluid to minimize beam deviations. The transmitted light is analyzed as a function of the translation distance of the incident beam. The retardation δ at the output provides the information on the stress distribution $\sigma_z(z)$ from an Abel integral equation [44],

$$\sigma_z(r) = -\frac{1}{\pi C}\int_r^R \frac{\delta'(y)}{\sqrt{y^2 - r^2}}\,dy, \tag{9.3.8}$$

where the prime indicates differentiation with respect to the transverse coordinate y, R is the radius of the fiber, and C is the stress-optic coefficient of silica. A change in the axial stress changes the refractive index by the stress-optic coefficient. The three components of the refractive index change, n_r, n_θ, and n_z, are related to the axial, circumferential, $\sigma_\theta(r)$, and radial, $\sigma_\rho(r)$ components of the stress-optic coefficients as [47]

$$\begin{aligned} n_r &= n_0 - B_2\sigma_r - B_1(\sigma_\theta + \sigma_z) \\ n_\theta &= n_0 - B_2\sigma_\theta - B_1(\sigma_r + \sigma_z) \\ n_z &= n_0 - B_2\sigma_z - B_1(\sigma_\theta + \sigma_z). \end{aligned} \tag{9.3.9}$$

In Eq. (9.3.9) the refractive index components are for light waves that have their electric field components in each of the three directions. The

refractive index of the fiber is n_0 without stress, and the stress-optic coefficients B_1 and B_2 are both positive, with $B_1 = 4.12 \times 10^{-5}$ mm^2 kg^{-1} and $B_2 = 0.64 \times 10^{-5}$ mm^2 kg^{-1} [48]. The radial component of the stress may be calculated from the axial component as [49]

$$\sigma_r(r) = \frac{1}{r^2}\int_r^R \sigma_z(s)sds. \tag{9.3.10}$$

The sign of the axial stress is found by measurements on silica fibers with and without strain, and through symmetry properties, $\sigma_r(r) = \sigma_\theta(r) = \sigma_z(r)/2$. The axial stress $\sigma_\theta(r)$ indicates positive axial tension for a positive sign and compressive strain with a negative sign.

By measuring the stress profile, the changes in the refractive index can be calculated as a function of the UV irradiation. Experiments performed by Fonjallaz *et al.* [46,50] have found that the axial stress increased with UV inscription of gratings, contrary to the stress-relief model [42]. The fibers are found to be either under slight axial compression or under tensile stress before UV irradiation (between -5 and $+1.6$ kg mm^{-2}). The stress changes before and after UV irradiation of a fiber with a Ge concentration of 12% are shown in Fig. 9.26. The maximum stress on the axis of the fiber is found to be 14.2 kg mm^{-2}. An increase in the tension

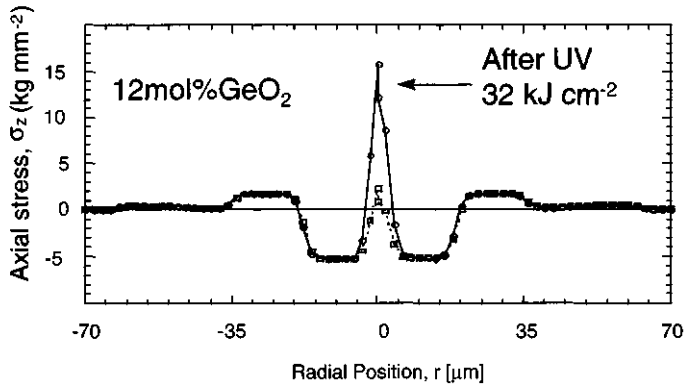

Figure 9.26: The measured radial stress profile of a fiber before and after the inscription of the grating (courtesy Hans Limberger [46]). (from: Fonjallaz P Y, Limberger H G, Salathé, Cochet F and Leuenberger B, "Tension increase corellated to refractive index change in fibers containing UV written Bragg gratings", *Opt. Lett.*, *20*(11), 1346–1348, 1 June 1995.)

is equivalent to a reduction in the refractive index; the implication is that the stress changes counter the overall change in the UV-induced refractive index, since this is *positive* (the Bragg wavelength moves to longer wavelengths with increase in refractive index of the core).

The net result of tension increase is that approximately 30% of the UV-induced refractive index change is *negative* and other factors, presumably compaction and changes in the UV absorption spectrum, increase the overall refractive index [51].

9.4 Strength, annealing, and lifetime of gratings

Reliability of fiber Bragg gratings is essential for long-term usage in telecommunications. There are two aspects that need to be taken into account: the mechanical strength and longevity of the grating. Mechanical strength of optical fiber is degraded through intense UV exposure, while the strength of the refractive index modulation of the grating begins to decay from the time of fabrication. The decay is slow but of concern unless treated. Careful handling and packaging of the UV-exposed grating may preserve the mechanical strength component.

The issue of mechanical strength is common with the deployment of optical fibers; they need to be tested to assure 25-year survivability. The process of grating inscription generally requires the removal of the protective primary coating of the fiber prior to exposure. While a special polymer may be used for through coating inscription [52], this is not generally the case. The mechanical removal damages the surface unless chemical means are used [53]. UV exposure can further reduce the strength [54]. Some form of protective coating must be applied to conserve the strength, if the fiber is to be handled mechanically [55].

9.4.1 Mechanical strength

The issue of mechanical reliability of in-fiber Bragg gratings has been extensively studied [56–58]. The degradation in the strength of a fiber is due to the growth of cracks on the surface at tiny flaws. Stress concentration at these flaws propagates and causes the fiber to fail. The failure strength can be dramatically lowered over that of pristine fiber. A convenient method of comparing the strength of different fibers is by the mea-

surement of dynamic fatigue. From the dynamic fatigue tests it is possible to predict the lifetime to failure by determining the distribution of flaws. The strength of optical fiber exposed to pulsed KrF radiation is dramatically reduced from a mean breaking strength of ~4.8 GPa for pristine fiber to 1.2 GPa. Recoating the fiber immediately after exposure restores the breaking strength. With CW 244-nm radiation, the strength is almost unchanged [59], but the long-term survivability is compromised, while hydrogen loading has little influence on the breaking strength. For a failure probability of 1×10^{-3}, the operational stress must be less than ~1 GPa for a 20-year lifetime [59], using a test length of 100 mm and a grating of ~8 mm.

9.4.2 Bragg grating lifetime and thermal annealing

The thermal stability of Bragg gratings is of prime importance if fabricated components are to function properly over their required life. For example, the a reduction in the reflectivity of a fiber Bragg grating used in an add–drop multiplexer from 40 to 30 dB could cause a degradation in crosstalk between channels. It is therefore essential to be able not only to predict the decay of the grating strength, but also to find ways to stabilize it.

Experimental observations of the decay in the reflectivity of gratings have resulted in a model that predicts the lifetime of gratings. It is generally agreed that observations on all fibers other than hydrogen-loaded follow a power-law dependence, originally proposed by Erdogan *et al.* [60,61]. The essential differences are the exact values of the coefficients that are used in the model.

The model proposes that the coupling constant of a grating $\kappa_{ac}L$ decays according to the following power law:

$$\eta = \frac{\kappa_{ac}L}{\kappa_{ac}L|_{t=0}} = \frac{1}{1 + At^{\alpha}}. \tag{9.4.1}$$

Here the denominator on the LHS is the initial value of the coupling constant at the time of writing of the grating. The constants A and α are temperature dependent and are found by plotting the normalized coupling constant η as a function of time. For convenience, the time parameter t may be normalized by unit time, e.g., 1 min to make Eq. (9.4.1) dimensionless. By measuring the decay of several gratings at different tempera-

tures as a function of time, and fitting the data with Eq. (9.4.1), the values of A and η can be evaluated for a particular fiber.

According to the model, the exponent $\alpha = T/T_0$ and $A = A_0 e^{aT}$, so that T_0 is the fitted parameter when α is evaluated. Based on a theoretical approach, the model assumes that there is a distribution of trapped states after UV exposure (distribution of induced defects, DID). The thermal depopulation of these states into the conduction band has a release rate that is dependent on temperature and the energy E as

$$\nu(E) = \nu_0 e^{-E/k_B T}, \tag{9.4.2}$$

where k_B is the Boltzmann constant. States below the demarcation energy E_d may be easily depopulated at a given temperature T. The time taken to decay is related to the demarcation energy as

$$t \approx \frac{1}{\nu(E_d)}. \tag{9.4.3}$$

In Fig. 9.27 is shown the decay of the normalized coupling constant of gratings elevated to three different temperatures, Equation (9.4.1) can be expressed in terms of the release rate as

$$\eta = \frac{1}{1 + [\nu(E)t]^{\alpha}}. \tag{9.4.4}$$

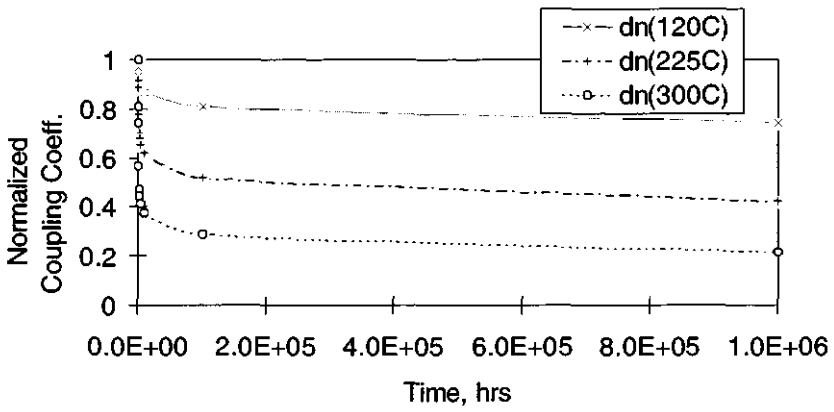

Figure 9.27: The thermal decay of boron–germanium codoped fibers, computed from the fitted data [62].

Using Eqs. (9.4.2)–(9.4.4), a Fermi–Dirac function describes the decay in the normalized coefficient,

$$\eta = \frac{1}{1 + e^{(E_d - E_0)/k_B T_0}}, \tag{9.4.5}$$

where E_0 is the peak of the distribution. We note that $A = v(E)^{\alpha}$ and is dependent on the release rate at energy E and on α. The distribution of the defects (DID) is calculated from Eqs. (9.4.2) and (9.4.5) and is

$$g(E) = \frac{N(0)}{k_B T} \frac{e^{(E - E_0)/k_B T_0}}{[1 + e^{(E - E_0)/k_B T_0}]^2}. \tag{9.4.6}$$

In Figure 9.27 is plotted the decay of the normalized coupling constant as a function of time for three different values of temperature [62]. The trend in the decay of the strength of gratings is typical. However, the magnitudes vary greatly. The computed A values from the fitted data to curves such as in Fig. 9.27 give the result shown in Fig. 9.28 in which a linear relationship may be seen when A is plotted on a logarithmic scale. This also ensures the validity of the data.

Alpha is similarly plotted in Fig. 9.29. Again, the linearity of the data should be such that it should pass through zero.

It turns out that the dependence of the decay of hydrogen-loaded boron-germanium fibers is much faster than that of unloaded fibers [62,63]. It has been speculated by the use of a more complex model that the DID in hydrogen-loaded fibers is not a single Gaussian distribution but a flat top [64,65]. It has also been suggested that the distribution

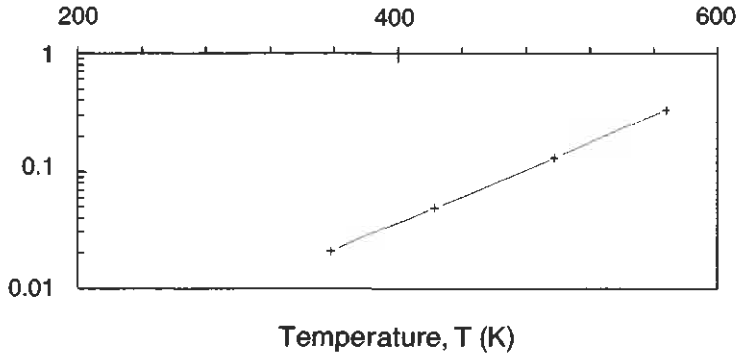

Figure 9.28: Relationship between A and the annealing temperature [62].

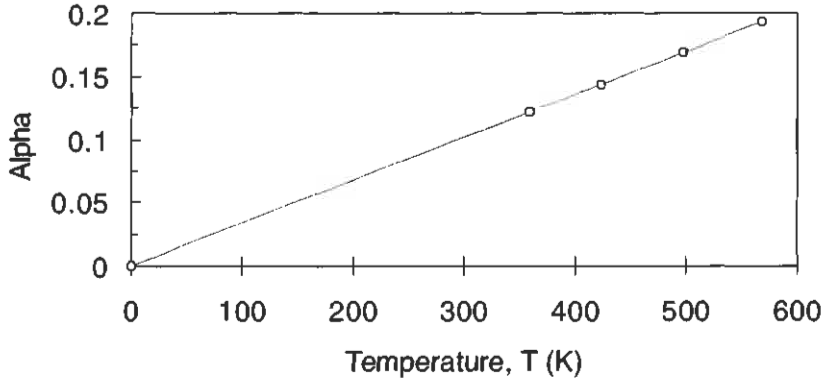

Figure 9.29: The fitted α to data on boron–germanium codoped fiber [62].

may be expressed as a stretched exponential [66]. However, there is no consensus as to a valid model. Riant *et al.* have pointed out the existence of at least two DIDs, and these are shown in Fig. 9.30. The contribution of each DID changes with temperature. It seems sensible that there may be several such DIDs, which play a role in determining the exact nature of the thermal decay of gratings.

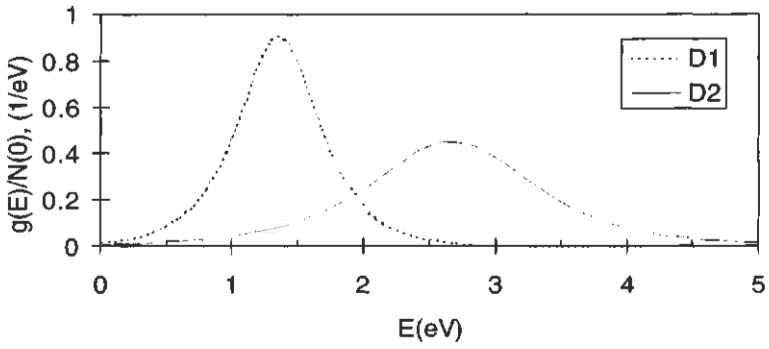

Figure 9.30: The distribution of the energy states of two DIDs in hydrogen-loaded fibers [67]. One defect is centered at 1.35 eV and has a narrow distribution, whereas the second, at 2.67 eV, has a much broader distribution.

9.4.3 Accelerated aging of gratings

Annealing a grating at an elevated temperature for a short time removes the fast decay, so that at lower temperatures, the decay rate slows down. This is the principle of accelerated aging [60,68]. The relationship between the annealing temperature T_2 and the lifetime of a grating operated at temperature T_1 is given by the simple relationship

$$t_2 = e^{aT_0[(T_1/T_2)-1]} t^{T_1/T_2}, \tag{9.4.7}$$

where the annealing time is t_2 and the time over which the grating is to be used is t_1. The parameter a has been defined in section 9.4.2.

The data for boron–germanium codoped fiber [62] with $a = 1.31 \times 10^{-2}\ \mathrm{K}^{-1}$ and $T_0 = 2941$ K is shown in Fig. 9.31, for an expected grating lifetime of 25 years at 300 K. The relationship between the time of annealing and the anneal temperature shows that annealing at 480 K for 1 min is equivalent to 25 years at 300 K. In order to ensure that the grating meets the specification for the application, this initial "burning-in" phase must be taken into account, since there is a reduction in the refractive index modulation.

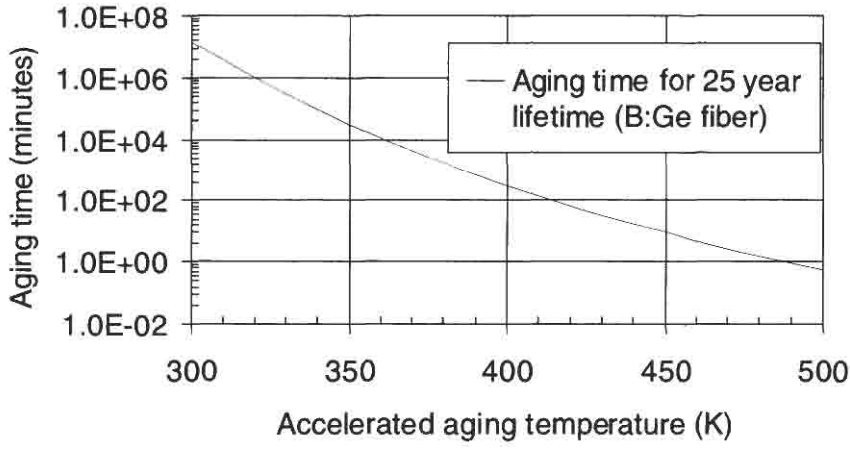

Figure 9.31: Accelerated aging characteristics of boron-germanium co-doped fiber [62], for a predicted lifetime of 25 years.
Accelerated aging characteristics of boron-germanium co-doped fiber [62], for a predicted lifetime of 25 years.

References

1. Mizrahi V. and Sipe J. E., "Optical properties of photosensitive fiber phase gratings," *J. Lightwave Technol.* **11**(10), 1513–1517 (1993).
2. Kashyap R., McKee P. F., Armes D. J., Shabeer M., and Cotter D. C., "Measurement of ultra-steep edge, high rejection fibre Bragg grating filters," *Electron. Lett.* **31**(15), 1282–1283 (1995).
3. Martin J., Lauzon J., Thibault S., and Ouellette F., "Novel writing technique of long highly reflective in fiber gratings and investigation of the linearly chirped component," post-deadline paper PD29-1, 138, *Proc. Conference on Optical Fiber Communications, OFC '94,* (1994).
4. Kashyap R., M. de Lathouwer, Emplit Ph, Haelterman M., Campbell R. J., and Armes D. J., "Dark soliton generation using a fibre Bragg grating," Photosensitivity and Quadratic Nonlinearity in Glass Waveguides: Fundamentals and Applications, OSA Annual Meeting, Oregon, 9–11 September, 1995.
5. Carballar A. and Muriel M. A., "Phase reconstruction from the reflectivity in fiber Bragg gratings," *J. Lightwave Technol.* **15**(8), 1314–1322 (1997).
6. Campbell R. J. and Kashyap R., "Spatial refractive index distribution of self-organized Bragg gratings in germanosilicate fiber," in *Tech. Digest of the Optical Soc. Am. Annual Meeting, OSA '93,* p. 148 (1993).
7. Ohn M. M., Huang S. Y., Sandgren S., and Mesures R., "Measurement of fiber grating properties using an interferometric and Fourier transform based technique," in *Conf. on Optical Fib. Commun., OFC '97,* pp. 154–155 (1997).
8. Barcelos S., Zervas M. N., and Laming R., "Characterization of chirped fiber Bragg gratings for dispersion compensation," *Opt. Fiber Technol.,* 213–215 (1996).
9. Sandel D. and Noé R., "Chirped fiber Bragg gratings for optical dispersion compensation: how to improve their fabrication accuracy," in *Tech. Digest of ECOC '96,* Vol. 2, pp. 233–236 (1996).
10. Hill K. O., Bilodeau F., Malo B., Kitagawa T., Theriault, Johnson D. C., and Albert J., "Aperiodic in fibre gratings for optical fiber dispersion compensation," in *Technical Digest of Post Deadline papers,* PD2-1, *Proc. Conference on Optical Fiber Communications, OFC '94,* (1999).
11. Devaux F., Sorel Y., and Kerdlies J. F., "Simple measurement of fiber dispersion and chirp parameter of intensity modulated light emitter," *J. Lightwave Technol.* **11**(12), 1937–1940 (1993).
12. Lauzon J., Thibault S., Martin J., and Ouellette O., "Implementation and characterization of fiber Bragg gratings linearly chirped by a temperature gradient," *Opt. Lett.* **19**(23), 2027–2029 (1994).

13. Roman J. E., Frankel M. Y., and Esman R. D., "High resolution technique for characterizing chirped fiber gratings," in *Tech. Digest of Conf. on Opt. Fib. Commun., OFC '98,* pp. 6–7 (1998).

14. Brinkmeyer E., Stolze G., and Johlen D., "Optical space domain reflectometry (OSDR) for determination of strength and chirp distribution of fiber gratings," in *Bragg Gratings, Photosensitivity, and Poling in Glass Fibers and Waveguides: Applications and Fundamentals,* Vol. 17, OSA Technical Digest Series (Optical Society of America, Washington, DC, 1997), paper BSuC2, pp. 33–35.

15. Nykolak G., Lenz G., Eggleton B. J., and Strasser T. A., "Impact of grating dispersion on WDM system performance," in *Tech. Digest of Conference on Optical Fiber Communications, OFC '98,* paper TuA3, pp. 4–5 (1998).

16. Sipe J. E., Eggleton B. J., and Strasser T. A., "Evolution of transmission dispersion characteristics of nonuniform gratings for DWDM systems," *ibid.,* paper TuA2, 3–4 (1998).

17. Lacerda-Rocha M. and Kashyap R., "Repeatability in the characterization of chirped Bragg gratings," in *Proc. Optical Fibers Measurements Conference, OFMC '98,* (1998).

18. Kashyap R. and Reeve M. H., "Single ended fibre strain and length measurement in the frequency domain," *Electron. Lett.* **16**(18), 689–690 (1980).

19. Kashyap R., Swanton A., and Armes D. J., "A simple technique for apodising chirped and unchirped fibre Bragg gratings," *Electron. Lett.* **32**(14), 1226–1228 (1996).

20. Malo B., Albert J., Kill K. O., Bilodeau F., and Johnson D. C., "Effective index drift from molecular hydrogen loaded optical fibres and its effect on Bragg *grating fabrication," Electron. Lett.* **30**(5), 442–444 (1994).

21. Bhakti F., Larrey J., Sansonetti P., and Poumellec B., "Impact of in-fiber and out-fiber diffusion on central wavelength of UV-written long period gratings," in *Bragg Gratings, Photosensitivity and Poling in Glass Fibers and Waveguides: Fundamentals and Applications,* Vol. 17, 1997 OSA Technical Series (Optical Society of America, Washington, DC, 1997), paper BSuD2, pp. 55–57 (1997).

22. Ouellette F. and Stephanov D. Y., "A new technique for measuring the group delay of chirped fiber Bragg gratings," in *Tech. Digest of Conf. on Opt. Fiber Commun., OFC '97,* pp. 153–154 (1997).

23. Meltz G. and Morey W. W., "Bragg grating formation and germanosilicate fiber photosensitivity," in *SPIE* **1516**, pp. 185–199 (1991).

24. Erdogan T. and Mizrahi V., "Characterization of UV induced birefringence in photosensitive Ge-doped silica optical fibers," *J. Opt. Soc. Am. B* **11**(10), 2100–2105 (1994).

25. Bonino S., Norgia M., Riccardi E., and Schiano M., "Measurement of polarisation properties of chirped fibre gratings," in *Technical Digest of OFMC '97,* pp. 10–13 (1997).

26. Ellis A. D., Kashyap R., Crisp I., Malyon D. J., and Heuting J. P., "Demonstration of an 80 Gb/s throughput reconfigurable dispersion compensating WDM Adm using deuterium sensitised 10 cm step chirped fibre Bragg gratings," in *Proc. of ECOC '97,* (1997).

27. Ouellette F., Krug P. A., and Pasman R., "Characterisation of long phase masks for writing fibre Bragg gratings," *Optical Fiber Technol.* **2**, 281–284 (1996).

28. Takada K., Yokohama I., Chida K., and Noda J., "New measurement system for fault location in optical waveguide devices based on an interferometric technique," *Appl. Opt.* **26**, 1603–1606 (1987).

29. Danielson B. L. and Wittenberg C. D., "Guidedwave reflectometry with micrometer resolution," *Appl. Opt.* **26**, 2836–2842 (1987).

30. Lambelet P., Fonjallaz P. Y., Limberger H. G., Salathé R. P., Zimmer C., and Gilgen H. H., "Bragg grating characterization by optical low-coherence reflectometry," *IEEE Phot. Technol. Lett.* **5**, 565–567 (1993).

31. Krug P., Stolte R., and Ulrich R., "Measurement of index modulation along an optical fiber Bragg grating," *Opt. Lett.* **20**(17), 1767–1769 (1995).

32. Margulis W., Carvalho I. C. S., and Govea P. M. P., "Heat scan: a simple technique to study gratings in fibers," *Opt. Lett.* **18**(12), 1016–1018 (1998).

33. Sandgren S., Sahlgren B., Asseh A., Margulis W., Laurell F., Stubbe R., and Lidgard A., "Characterization of Bragg gratings in fibers with the heat-scan technique," *Electron. Lett.* **31**, 665–666 (1995).

34. Loh W. H., Cole M. J., Zervas M. N., and Laming R. I., "Compensation of imperfect mask with moving fibre-scanning beam technique for production of fibre gratings," *Electron. Lett.* **31**(17), 1483–1485 (1995).

35. Ouellette F., Krug P. A., and Pasman R., "Characterisation of long phase masks for writing fibre Bragg gratings," in *Photosensitivity and Quadratic Nonlinearity in Glass Waveguides: Fundamentals and Applications,* Vol. 22, 1995 OSA Technical Series (Optical Society of America, Washington, DC, 1995), pp. 116–119.

36. Ouellette F., "The effect of profile noise on the spectral response of fiber gratings," in *Bragg Gratings, Photosensitivity, and Poling in Glass Fibers and Waveguides: Applications and Fundamentals,* Vol. 17, OSA Technical Digest Series (Optical Society of America, Washington, DC, 1997), paper BMG13, pp. 222–224.

37. Limberger H. G., Fonjallaz P. Y., Lambelet P., Salathé R. P., Zimmer C., and Gilgen H. H., "Fiber grating characterization by OLCR measurements," *European Conference on Optical Fibre Communications,* paper MoP2.1 (1993).

38. Malo B., Thériault S., Johnson D. C., Bilodeau F., Albert J., and Hill K. O., "Apodised in-fibre Bragg grating reflectors photoimprinted using a phase mask," *Electron. Lett.* **31**(3), 223–225 (1995).

39. Fonjallaz P. Y., Limberger H. G., and Salathé R. P., "Bragg grating with directional, efficient and wavelength selective fiber out coupling," in *Tech. Digest of Opt. Fiber Commun., OFC '95,* paper WN3, pp. 160–161 (1995).

40. Archambault J-L., Reekie L., and Russell P. St. J., "100% reflectivity Bragg reflectors produced in optical fibres by single excimer pulses," *Electron. Lett.* **29**(5), 453 (1993).

41. Janos M., Canning J., and Sceats M. G., "Incoherent scattering losses in optical fiber Bragg gratings," *Opt. Lett.* **21**(22), 1827–1829 (1996).

42. Sceats M. G. and Krug P., "Photoviscous annealing — dynamics and stability of photorefractivity in optical fibers," in *SPIE* **2044**, 113–120 (1993).

43. See, for example, Douay M., Xie W. X., Taunay T., Bernage P., Niay P., Cordier P., Poumellec B., Dong L., Bayon J. F., Poignant H., and Delevaque E., "Densification involved in the UV based photosensitivity of silica glasses and optical fibers," *J. Lightwave Technol.* **15**(8), 1329–1342 (1997).

44. Chu P. L. and Whitbread T., "Measurement of stress in optical fiber and preform," *Appl. Opt.* **21**, 4241–4245 (1982).

45. Bachmann P. K., Hermann W., Wher H., and Weichert D. U., "Stress in optical waveguides. 1: Preforms," *Appl. Opt.* **25**(7), 1093–1098 (1986).

46. Fonjallaz P. Y., Limberger H. G., Salathé R. P., Cochet F., and Leuenberger B., "Tension increase correlated to refractive index change in fibers containing UV written Bragg gratings," *Opt. Lett.* **20**(11), 1346–1348 (1995).

47. Scherer G. W., "Stress-induced index profile distribution in optical waveguides," *Appl. Opt.* **19**, 2000 (1980).

48. Primark W. and Post D., "Photoelastic constants of vitreous silica and its elastic coefficient of refractive index," *J. Appl. Phys.* **30**, 779 (1959).

49. Hermann, Hutjens W. and Wiechert D. U., "Stress in optical waveguides. 3: Stress induced index changes," *Appl. Opt.* **28**, 1980–1983 (1989).

50. Limberger H. G., Fonjallaz P. Y., Salathé R. P., and Cochet F., "UV induce stress changes in optical fibers," in *Photosensitivity and Quadratic Nonlinearity in Glass Waveguides: Fundamentals and Applications,* Vol. 22, 1995 OSA Technical Series (Optical Society of America, Washington, DC, 1995), paper SAD4, pp. 56–60.

51. Limberger H. G., Fonjallaz P. Y., Salathé R. P., and Cochet F., "Compaction- and photoelastic-induced index changes in fiber Bragg gratings," *Appl. Phys. Lett.* **68**, 3069–3071 (1996).

52. See, for example, Starodubov D. S., Grubsky V., Feinberg J., Dianov D., Semjonov S. L., Guryanov A. N., and Vechkanov N. N., "Fiber Bragg gratings with reflectivity >97% fabricated through polymer jacket using near-UV radiation," in *Bragg Gratings, Photosensitivity, and Poling in Glass Fibers and Waveguides: Applications and Fundamentals,* Vol. 17, OSA Technical Digest Series (Optical Society of America, Washington, DC, 1997), post-deadline paper PD1.

53. Limberger H. G., Valeras D., Salathé R. P., and Kotrotsios, "Mechanical degradation of optical fibers induced by UV light," *Proc. SPIE* **2841**, 84–93 (1996).

54. Feced R., Roe-Edwards M. P., Kanellopoulos S. E., Taylor N. H., and Handerek V. A., "Mechanical strength degradation of UV exposed optical fibres," *Electron. Lett.* **33**(2), 157–159, 16 January 1997.

55. Putnam M. A., Askins C. G., Smith G., and Fribele E. J., "Method for recoating fiber Bragg gratings with polyimide," in *Industrial and Commercial Applications of Smart Structures Technology,* Slater J. A., Vol. 2044 pp. 359–362. SPIE, Bellingham, WA (1997).

56. Kapron F. P. and Yuce H. H., "Theory and measurement for predicting stressed fiber lifetime," *Opt. Eng.* **30**(6), 700–708 (1991).

57. Mitsunaga Y., Katsuyama Y., Kobayashi H., and Ishida Y., "Failure prediction for long-length optical fibers based on proof testing," *J. Appl. Phys.* **53**(7), 700 (1982).

58. See, for example, *Proc. of the First European COST Workshop 246 on Bragg grating Reliability,* IOA-EPFL (1995).

59. Limberger H. G., Valeras D., and Salathé R. P., "Reliability aspects of fiber Bragg gratings," in *Proc. of Optical. Fibre Meas. Conf., OFMC '97,* 18–123 (1997).

60. Erdogan T. and Mizrahi V., "Decay of UV induced fiber Bragg gratings," *Proc. Optical Fiber Conference, OFC '94,* p. 50 (1994).

61. Erdogan T., Mizrahi V., Lemaire P. J., and Monroe D., "Decay of ultraviolet-induced fiber Bragg gratings," *J. Appl. Phys* **76**(1), 73–80 (1994).

62. Baker S. R., Rourke H. N., Baker V., and Godchild D., "Thermal decay of fiber Bragg gratings written in boron and germanium codoped silica fiber," *J. Lightwave Technol.* **15**(8), 1470–1477 (1997).

63. Patrick H., Gilbert S. L., Lidgard A. and Gallagher M. D., "Annealing of Bragg gratings in hydrogen loaded optical fibers," *J. Appl. Phys.* **78**(5), 2940–2945 (1995).

64. Guo J. Z. Y., Kannan S. and Lemaire P. J., "Thermal stability of optical add/drop gratings for WDM systems," in *Tech. Digest of OFC '97,* paper ThJ6, pp. 285 (1997).

65. Kannan S., Gou J. Z. Y., and Lemaire P. J., "Thermal reliability of strong Bragg gratings written in hydrogen sensitized fibers," in *Tech. Digest of OFC '97* paper TuO4, pp. 84–85 (1996).

66. Egan R. J., Inglis H. G., Hill P., Krug P. A., and Ouellette F., "Effects of hydrogen loading and grating strength on the thermal stability of fiber Bragg grating," in *Tech. Digest of OFC '96,* paper TuO3, pp. 83–84 (1996).

67. Robert G. and Riant I., "Demonstration of two distributions of defect centers in hydrogen loaded high germanium content fibers," in *Tech. Digest of OFC '97,* paper WL18, pp. 180–181 (1997).

68. Williams D. L. and Smith R. P., "Accelerated lifetime tests on UV written intracore gratings in boron germanium co-doped silica fibre," *Electron. Lett.* **31**(24), 2120–2121 (1995).